molecules

MDPI

Article

Composite ZIF-8 with $Cs_3Bi_2I_9$ to Enhance the Photodegradation Ability on Methylene Blue

Tao Tang [1,2], Haoran Zhang [1], Hexu Wang [1], Xiaoyu Dou [1], Jianfeng Wen [1,*] and Li Jiang [1,*]

[1] Key Laboratory of Low-Dimensional Structural Physics and Application, Education Department of Guangxi Zhuang Autonomous Region, College of Physics and Electronic Information Engineering, Guilin University of Technology, Guilin 541004, China; tangtao@glut.edu.cn (T.T.); glzhanghaoran@163.com (H.Z.); wanghx0907@163.com (H.W.); douxiaoyu1018@163.com (X.D.)

[2] School of Electronic Information and Automation, Guilin University of Aerospace Technology, Guilin 541004, China

* Correspondence: wjfculater@163.com (J.W.); jiangli1515@glut.edu.cn (L.J.)

Abstract: The development of green, efficient, and reusable photocatalysts is important for pollution degradation. In recent years, $Cs_3Bi_2I_9$ has been shown to be an effective photocatalyst. However, the rapid recombination of electrons and holes weakens the photocatalytic activity. In this work, the photogenerated electron transfer rate was promoted by ZIF-8 compositing with $Cs_3Bi_2I_9$, which effectively improved the pollutant degradation. After 50 min of visible light irradiation, $Cs_3Bi_2I_9$/ZIF-8 removed up to 98.2% of methylene blue (MB), which was 4.15 times higher than that of $Cs_3Bi_2I_9$ alone. In addition, the $Cs_3Bi_2I_9$/ZIF-8 composite still exhibited high photocatalytic activity after three cycling experiments. Our research offers a simple and efficient method for enhancing the photocatalytic activity of lead-free halide perovskites.

Keywords: photocatalysis; lead-free perovskites; $Cs_3Bi_2I_9$; ZIF-8

check for updates

Academic Editor: Lagnamayee Mohapatra

Received: 17 February 2025
Revised: 12 March 2025
Accepted: 19 March 2025
Published: 22 March 2025

Citation: Tang, T.; Zhang, H.; Wang, H.; Dou, X.; Wen, J.; Jiang, L. Composite ZIF-8 with $Cs_3Bi_2I_9$ to Enhance the Photodegradation Ability on Methylene Blue. *Molecules* **2025**, *30*, 1413. https://doi.org/10.3390/molecules30071413

Copyright: © 2025 by the authors. Licensee MDPI, Basel, Switzerland. This article is an open access article distributed under the terms and conditions of the Creative Commons Attribution (CC BY) license (https://creativecommons.org/licenses/by/4.0/).

1. Introduction

While actively promoting industrialization, countries have also brought tremendous challenges to environmental protection and resource conservation [1–3]. In recent years, the excessive use of various chemical reagents in the pharmaceutical, agricultural, and manufacturing industries has led to increasingly serious environmental pollution, which is contrary to the original intent of sustainable development [4–6]. Among these chemicals, methylene blue (MB) is a typical organic pollutant. Its aqueous solution is alkaline and harmful, causing serious environmental problems due to its non-biodegradation and accumulation in the environment [7]. The common strategies used to treat MB in wastewater are adsorption [8], biodegradation [9], and photocatalytic degradation [10]. Adsorption methods mainly suffer from high costs and secondary pollution issues, while biodegradation methods have long degradation cycles and strict restraint of degradation environments. In contrast, photocatalytic degradation of MB is the most efficient, environmentally friendly, and practical method.

Many materials such as TiO_2 [11], ZnO [12], CuO [13], Fe_2O_3 [14], ZnS [15], and graphene [16] have been widely used for photocatalytic degradation [17–19]. However, wide bandgap, low visible light utilization, and fast recombination of photogenerated electron and hole pairs are potential limitations that restrict the photocatalytic activity. Recently, lead-based perovskites have been shown to be an efficient visible-light photocatalyst [20–22]. However, the toxicity of lead and instability of these perovskites have

hindered its application in photocatalysis [23,24]. Guo et al. used a novel photocatalyst $CsPbBr_3$/UiO-66 to degrade 91.6% of 10 mg/L methyl orange in 90 min under visible light [25]. Gu et al. used nitrogen-doped graphene quantum dots as surfactants to prepare δ-phase $CsPbI_3$ nanocrystals and degraded 96% of rhodamine B in 4 h [26]. Although water stability can be improved by ligand exchange and surface functionalization, it is more important to develop lead-free halide perovskite photocatalysts that are non-toxic and water-stable [27]. In recent years, bismuth-based perovskites [28], which combines low toxicity with excellent water stability, have been discovered in the family of non-lead halide perovskites. In particular, a pioneering study by Sagar M. Jain et al. who chose lead-free bismuth-based perovskite $(CH_3NH_3)_3Bi_2I_9$ for the preparation of solar cells, successfully converted solar energy into electric energy, achieving a conversion efficiency of 22.3%, which attracted widespread attention [29]. This breakthrough not only highlights the great potential of bismuth-based perovskites in the field of solar energy conversion but also heralds their important role as efficient photocatalysts.

Among them, inorganic halide perovskite $Cs_3Bi_2I_9$ has attracted much attention due to its fast carrier transport, high defect tolerance, very low defect density, high water stability, and low toxicity [30–32]. Its photoluminescence quantum yield is 2.3% [33]. Effectively separating these electron-hole (e-h) pairs and transferring carriers is a feasible method to increase the number of carriers participating in photocatalysis [34–36]. Dou et al. demonstrated excellent stability by using $Cs_3Bi_2I_9$ composited with Ti_3C_2 and showed more than 97.3% rhodamine B removal efficiency under visible light [37]. Therefore, it is proved feasible to find a co-catalyst to enhance the rapid separation and transfer of photoexcited e-h pairs in $Cs_3Bi_2I_9$ to improve the photocatalytic performance [38,39]. In recent years, ZIF-8 has been used in electron transport layers due to its simple synthesis method, good conductivity, good stability, large specific surface area, high carrier mobility, and abundant active center sites [40].

In this study, the photocatalytic degradation performance of MB in aqueous solution was investigated by using $Cs_3Bi_2I_9$/ZIF-8 composites as photocatalysts. When ZIF-8 is combined with $Cs_3Bi_2I_9$, ZIF-8 provides abundant charge transfer channels, and the photogenerated electrons in $Cs_3Bi_2I_9$ can be rapidly transferred to the surface of ZIF-8, which is conducive to the effective transfer and separation of photogenerated carriers [41–43], thus greatly improving the photocatalytic efficiency of $Cs_3Bi_2I_9$. Under visible light, $Cs_3Bi_2I_9$/ZIF-8 can degrade 98.2% of MB (20 mg/L) within 50 min, much higher than $Cs_3Bi_2I_9$ (<50%), and there was almost no decrease in the photocatalytic activity after three cycles of the experiment. In addition, the fluorescence performance of $Cs_3Bi_2I_9$/ZIF-8 photocatalyst in water remains almost unchanged for 30 days, demonstrating its good water stability. This work demonstrates that, by compositing ZIF-8 with $Cs_3Bi_2I_9$, a highly efficient water-stable perovskite-based photocatalyst is obtained, which opens up prospects for the photocatalytic application of non-lead perovskites.

2. Results

The crystal structures of ZIF-8, $Cs_3Bi_2I_9$, and $Cs_3Bi_2I_9$/ZIF-8 were analyzed by XRD. The crystal structure of ZIF-8 characterized by XRD is shown in Figure 1a. The principal diffraction peaks of ZIF-8 are located at 2θ = 7.2°, 10.2°, 12.6°, 14.7°, 16.4°, 17.9°, 19.5°, 22.1°, 24.6°, 26.8°, 29.7°, 30.6°, which are attributed to the (001), (002), (112), (022), (013), (222), and (123) crystal planes, respectively [44]. The XRD patterns of $Cs_3Bi_2I_9$ and $Cs_3Bi_2I_9$/ZIF-8 are shown in Figure 1b. The diffraction peaks at 2θ = 21.11°, 25.84°, 27.52°, 29.72°, 32.35°, and 42.97°, respectively, correspond to (110), (202), (203), (204), (205), and (220) crystal planes of cubic-phase $Cs_3Bi_2I_9$ [45]. This indicates that both the synthesized ZIF-8 and $Cs_3Bi_2I_9$ exhibit high crystallinity and are consistent with the standard XRD patterns. In the XRD

pattern of $Cs_3Bi_2I_9$/ZIF-8, the characteristic peak at 7.2° attributed to ZIF-8 can be clearly resolved, while other peaks are overlapped with those belonging to $Cs_3Bi_2I_9$. These results suggest that ZIF-8 was successfully loaded onto $Cs_3Bi_2I_9$.

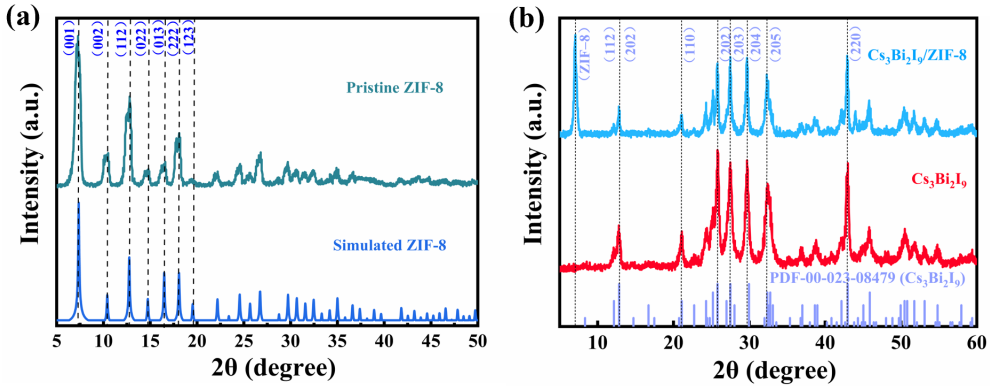

Figure 1. XRD patterns of (**a**) ZIF-8 and (**b**) $Cs_3Bi_2I_9$ and $Cs_3Bi_2I_9$/ZIF-8. The simulated and standard XRD patterns of ZIF-8 and $Cs_3Bi_2I_9$ are used for comparison.

The morphologies of the ZIF-8, $Cs_3Bi_2I_9$ and $Cs_3Bi_2I_9$/ZIF-8 can be clearly observed through SEM images. As shown in Figure 2a, it can be observed that ZIF-8 is a rhombic dodecahedral crystal with the particle size between 50 and 100 nm [46]. Figure 2b shows that $Cs_3Bi_2I_9$ exhibits a hexagonal structure with a larger lateral size of 200–400 nm. In the SEM image of $Cs_3Bi_2I_9$/ZIF-8 [Figure 2c], it is observed that small-size ZIF-8 regular particles were stacked on $Cs_3Bi_2I_9$ platelets. Figure 2d presents the typical TEM image of $Cs_3Bi_2I_9$/ZIF-8. The boundary of the blurred $Cs_3Bi_2I_9$ hexagon and the irregular boundary of ZIF-8 can be discernible. Through high-resolution TEM, two different lattice stripes of $Cs_3Bi_2I_9$ and ZIF-8 can be further clearly distinguished. The typical lattice spacings are 0.214 and 0.301 nm [Figure 2e,f], corresponding to the (101) crystal face of ZIF-8 and the (204) crystal face of $Cs_3Bi_2I_9$, respectively [47,48].

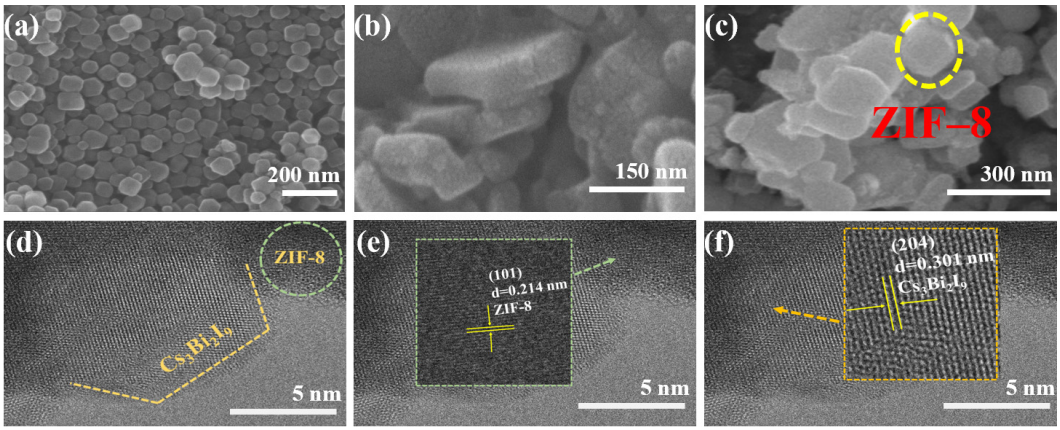

Figure 2. SEM images of (**a**) ZIF-8, (**b**) $Cs_3Bi_2I_9$, (**c**) $Cs_3Bi_2I_9$/ZIF-8. (**d**) High-resolution TEM image of $Cs_3Bi_2I_9$/ZIF-8. High-resolution TEM images of (**e**) ZIF-8 and (**f**) $Cs_3Bi_2I_9$ in $Cs_3Bi_2I_9$/ZIF-8 composite.

Water stability serves as a crucial indicator in assessing the suitability of a catalyst for applications in aqueous environments. As illustrated in Figure 3a, the water contact angles corresponding to $Cs_3Bi_2I_9$ and $Cs_3Bi_2I_9$/ZIF-8 are 43° and 88.7°, respectively. The significantly larger water contact angle observed for $Cs_3Bi_2I_9$/ZIF-8 suggests a reduced interaction surface with water. Thus, to some extent, it can be indirectly determined that $Cs_3Bi_2I_9$/ZIF-8 has a better water stability. Its optical properties were studied through UV-Vis absorption and PL tests. The band gap of ZIF-8 is 4.9 eV, which is insensitive

to the visible-region light [49]. In Figure 3b, the absorption properties of $Cs_3Bi_2I_9$/ZIF-8 are identical to those of $Cs_3Bi_2I_9$, with absorption edges up to 600 nm. Based on Tauc plots [50,51], the bandgap (E_g) of $Cs_3Bi_2I_9$ can be concluded to be 2.37 eV [inset of Figure 3b]. In Figure 3c, it is observed that the PL intensity of $Cs_3Bi_2I_9$/ZIF-8 is significantly stronger than $Cs_3Bi_2I_9$ with similar PL centers and shapes, and thus, it is demonstrated that many of the e-h pairs in $Cs_3Bi_2I_9$ no longer recombine in an emissive manner after ZIF-8 compositing. From the inset of Figure 3c, it can be noticed that the PL shape and intensity of $Cs_3Bi_2I_9$/ZIF-8 in water remain almost unchanged for 30 days, which indicates its excellent water stability. In addition, the arc radius of $Cs_3Bi_2I_9$/ZIF-8 is smaller than that of ZIF-8 and pure $Cs_3Bi_2I_9$ as measured by EIS [Figure 3d], suggesting that it possesses the lowest electron-transfer resistance, which is beneficial for the effective separation and migration of photogenerated carriers. In Figure 3e, the photocurrent response of $Cs_3Bi_2I_9$ is enhanced after ZIF-8 compositing under the same visible illumination, again indicating an increase in conducting carriers and a decrease in radiative recombination carriers. In a word, such experiments show that after ZIF-8 compositing, more photogenerated carriers in $Cs_3Bi_2I_9$ no longer undergo the radiative emission and can be effectively transferred to ZIF-8, which benefits their participation in the photocatalytic process.

ZIF-8 is a strong adsorbent which can almost completely adsorb some organic dyes within merely tens of minutes. However, by adsorption alone, MB is very hard to separate from water [52]. The high e-h recombination rate of $Cs_3Bi_2I_9$ gives rise to a relatively low photodegradation activity. When ZIF-8 is combined with $Cs_3Bi_2I_9$, the resulting composite exhibits enhanced effectiveness in the decontamination process for removing MB through the adsorption–photodegradation pathway [4]. As shown in Figure 4a, for ZIF-8, $Cs_3Bi_2I_9$ and $Cs_3Bi_2I_9$/ZIF-8, the adsorption–desorption equilibrium in the dark can be achieved in 2 h. One can find that the MB adsorption ability of $Cs_3Bi_2I_9$ is merely ~8% and that of ZIF-8 is ~13%, and however, that of $Cs_3Bi_2I_9$/ZIF-8 is slightly increased (~15%), which may be attributed to the increase in specific surface area due to the uniform distribution of ZIF-8 on $Cs_3Bi_2I_9$.

When ZIF-8 is composited with $Cs_3Bi_2I_9$, it provides more adsorption sites, which are able to capture and immobilize the target pollutants more efficiently, thus improving the adsorption efficiency. The increasing adsorption properties of CZ-1, CZ-2, and CZ-3 were attributed to the increase in ZIF-8 content. As illustrated in Figure 4b, it is evident that under visible light conditions, CZ-1, CZ-2, and CZ-3 exhibit photodegradation efficiencies of 86.3%, 93.4%, and 90.3%, respectively. When the content of ZIF-8 increased from 20 to 30 mg, the photocatalytic efficiency actually decreased, possibly due to too much ZIF-8 blocking the effective light absorption of $Cs_3Bi_2I_9$. As shown in Figure 4c, $Cs_3Bi_2I_9$/ZIF-8 shows an obviously higher MB photodegradation efficiency (93.4%) than $Cs_3Bi_2I_9$ (40%), and along with the adsorption, the total MB removal ratio of $Cs_3Bi_2I_9$/ZIF-8 (98.2%) is undoubtedly higher than that of sole $Cs_3Bi_2I_9$ (<50%). Compared with $Cs_3Bi_2I_9$, the improvement in photocatalytic performance of $Cs_3Bi_2I_9$/ZIF-8 is attributed to the effective separation and transfer of photo-generated carriers, as discussed in Figure 3. Interestingly, sole ZIF-8 exhibits very weak photodegradation ability on MB, may be due to its abundant active sites [47]. Fitting the corresponding photodegradation kinetics using a first-order reaction equation:

$$\ln\frac{C}{C_0} = -kt \quad (1)$$

where k is the photocatalytic efficiency (in this discussion its unit min^{-1} is omitted). As shown in Figure 4d, the k value of CZ-2 is 0.05, which is 4.15 times and 8.90 times of $Cs_3Bi_2I_9$ (k = 0.012) and ZIF-8 (k = 0.005), respectively. In order to investigate recycling property of the photocatalyst $Cs_3Bi_2I_9$/ZIF-8, three cycles of photocatalytic experiments

were conducted. As shown in Figure 4e, in the three cycles, the photodegradation efficiencies were 97%, 89%, and 85%, respectively. There is a slight decrease because the surface of $Cs_3Bi_2I_9$/ZIF-8 adsorbs MB molecules and it is hard to completely remove them. In order to determine the mechanism of the photocatalytic reaction, free radical trapping experiments were performed. As shown in Figure 4f, benzoquinone (BQ), isopropanol (IPA), silver nitrate ($AgNO_3$), and potassium iodide (KI) were used to capture superoxide radicals ($\bullet O_2^-$), hydroxyl radicals (•OH), electrons, and holes, respectively. There was no significant decrease in the catalytic activity of $Cs_3Bi_2I_9$/ZIF-8 in the presence of IPA and KI. However, when in the presence of $AgNO_3$ and BQ, the degradation of MB by $Cs_3Bi_2I_9$/ZIF-8 was merely 24% and 12%, respectively, indicating that the catalytic activity decreased greatly. This indicates that $\bullet O_2^-$ radicals and electrons were the main active substances during the photocatalytic degradation process.

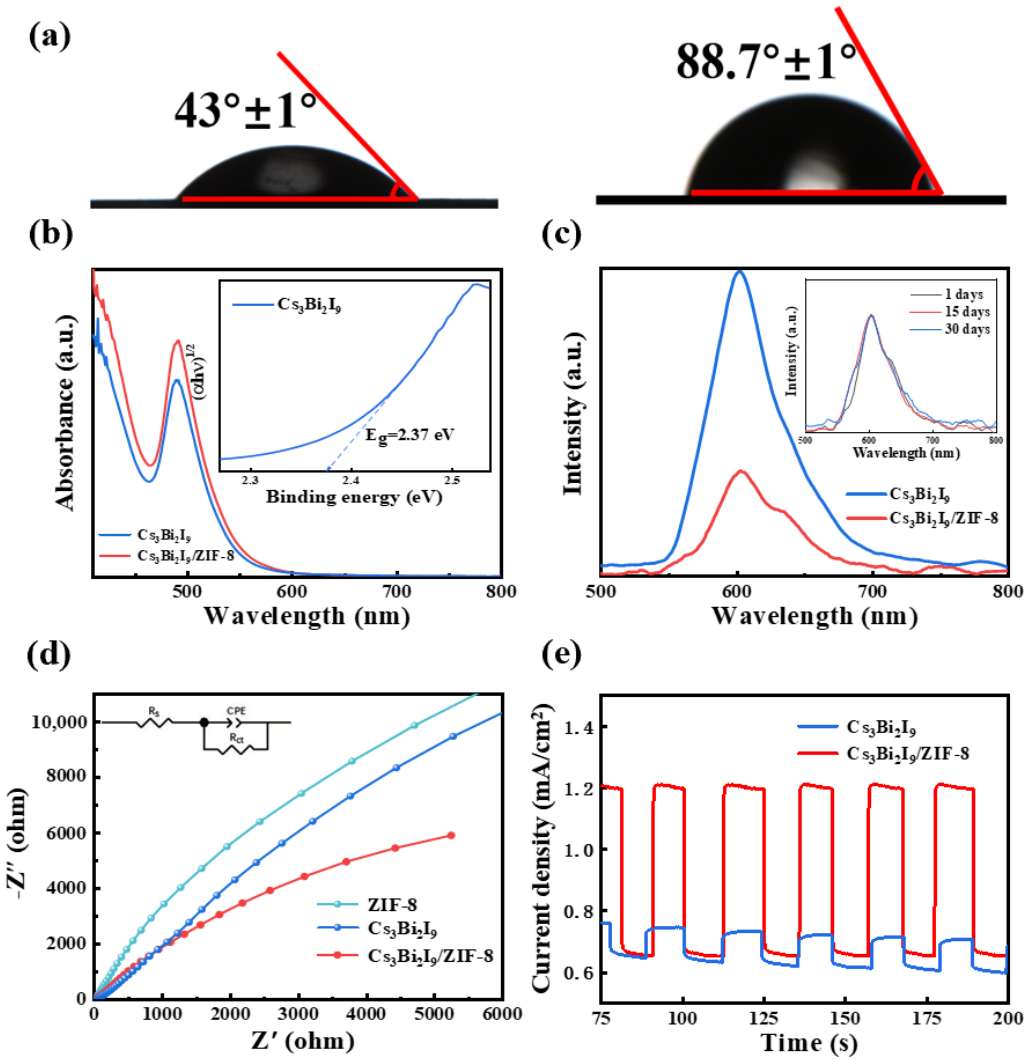

Figure 3. (**a**) Water contact angles of $Cs_3Bi_2I_9$ and $Cs_3Bi_2I_9$/ZIF-8. (**b**) UV–Vis absorption spectra of $Cs_3Bi_2I_9$ and $Cs_3Bi_2I_9$/ZIF-8. The inset is the corresponding Tauc plot of $Cs_3Bi_2I_9$. (**c**) PL spectra of $Cs_3Bi_2I_9$ and $Cs_3Bi_2I_9$/ZIF-8. The inset is the PL spectra of $Cs_3Bi_2I_9$/ZIF-8 on the 1st, 15th, and 30th day. (**d**) Electrochemical impedance measurements of ZIF-8, $Cs_3Bi_2I_9$ and $Cs_3Bi_2I_9$/ZIF-8. The inset is the equivalent circuit diagram, where R_s, R_{ct} and CPE denote the total resistance of the external circuit, the charge transfer resistance and constant phase element. (**e**) The visible-light photocurrent responses of $Cs_3Bi_2I_9$ and $Cs_3Bi_2I_9$/ZIF-8.

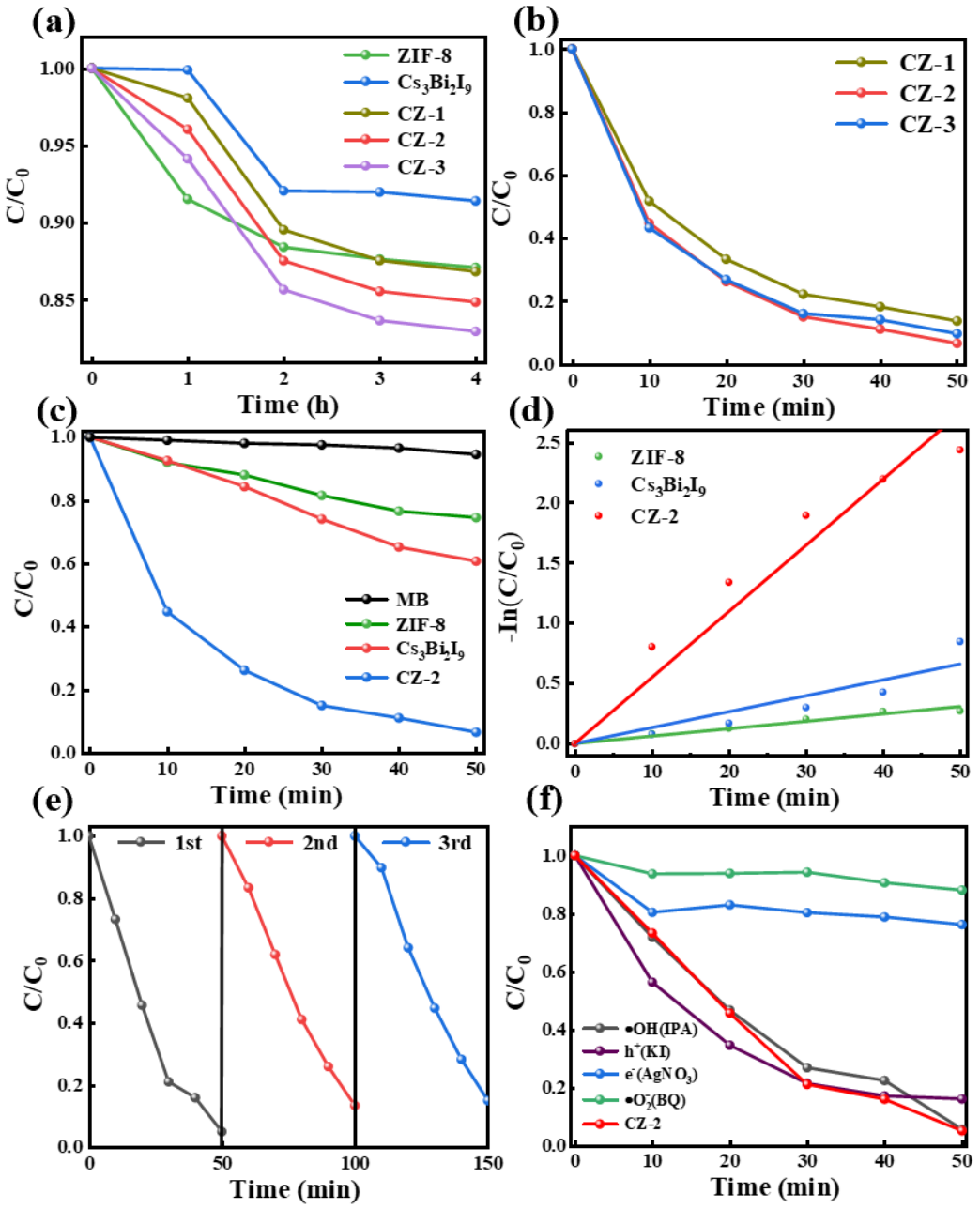

Figure 4. (**a**) The MB adsorption performances in the dark. (**b**) Photocatalytic degradation of MB of $Cs_3Bi_2I_9$/ZIF-8 with different ZIF-8 mass. (**c**) The MB photodegradation of different samples and (**d**) the corresponding photodegradation kinetics behavior. (**e**) Photocatalytic cycle tests of $Cs_3Bi_2I_9$/ZIF-8. (**f**) The impact of photocatalytic effect of $Cs_3Bi_2I_9$/ZIF-8 after scavengers addition.

In addition, Table 1 compares the relevant photocatalysts used for MB degradation in several studies. It can be seen that many photocatalysts can effectively degrade MB, but the photocatalytic time and degradation efficiency are not satisfactory. Compared with other photocatalyst materials, $Cs_3Bi_2I_9$/ZIF-8 can photodegrade high-concentration MB with a low dosage, as well as a high degradation efficiency with a short light exposure time. Obviously, $Cs_3Bi_2I_9$/ZIF-8 is a very promising photocatalyst.

Table 1. Comparison of MB degradation effects of photocatalysts under visible or UV Light.

Catalyst	Illumination	Quantity	C_0	Efficiency	Catalytic Time	Ref.
ZIF-8	Ultraviolet light	25 mg	10 mg/L	82.3%	120 min	[53]
$MnTiO_3$	Visible light	25 mg	10 mg/L	89.7%	180 min	[54]
$LaMnO_3$	Visible light	5 mg	5 mg/L	95%	120 min	[55]
MAIPb	Visible light	25 mg	10 mg/L	90%	60 min	[56]
$BiVO_4$	Visible light	0.25 g	5 mg/L	81%	240 min	[57]
TiO_2	Ultraviolet light	0.15 g	10 mg/L	81.4%	100 min	[58]
$Cs_3Bi_2I_9$/ZIF-8	Visible light	20 mg	20 mg/L	93.4%	50 min	This work

In order to investigate the mechanism of the photocatalysis, the valence band maxima (E_{VBM}) and conduction band minima (E_{CBM}) of ZIF-8 and $Cs_3Bi_2I_9$ were calculated by UPS measurements [Figure 5a] with $E_{VBM} = -[21.22 - (E_{cutoff} - E_{onset})]$. For ZIF-8, the E_{cutoff} was 15.48 eV and the E_{onset} was 3.31 eV. The E_{VBM} of ZIF-8 can be calculated as −9.05 eV according to the formula. Since the bandgap (E_g) of ZIF-8 is 4.9 eV, the E_{CBM} of ZIF-8 can be calculated as −4.55 eV according to the formula $E_g = E_{CBM} - E_{VBM}$ [59]. Typically, we use a standard hydrogen electrode (NHE) as a reference electrode to represent the energy levels, i.e., $E_{(NHE)} = -4.5 - E_{(vacuum)}$, to express the relationship between the NHE and the vacuum energy levels, which results in the VBM and CBM values of 4.55 eV and −0.35 eV, respectively. Similarly, the VBM and CBM values of $Cs_3Bi_2I_9$ were 2.01 eV and −0.39 eV, respectively, according to Figure 5a. Based on the above analysis, a possible mechanism for the photocatalytic removal of MB by $Cs_3Bi_2I_9$/ZIF-8 can be proposed [Figure 5b]:

$$h\nu \text{ (on } Cs_3Bi_2I_9) \rightarrow h^+ + e^- \quad (2)$$

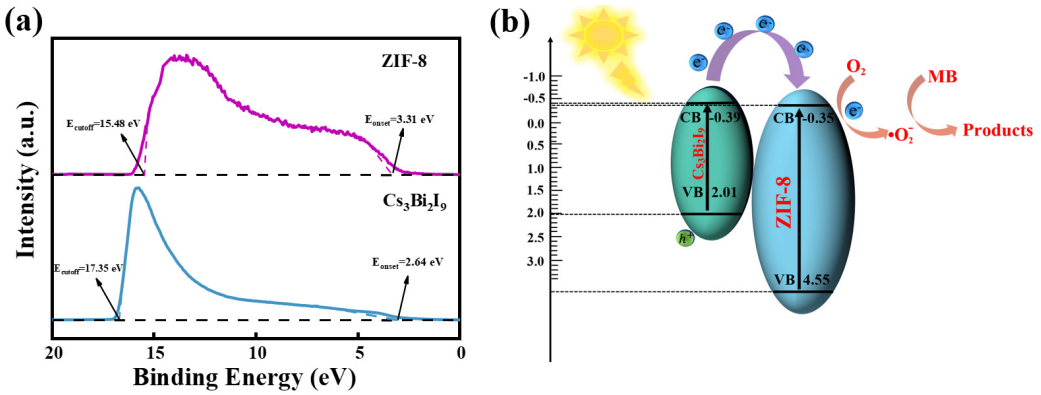

Figure 5. (**a**) UPS spectra of ZIF-8 and $Cs_3Bi_2I_9$. (**b**) The mechanism of photocatalytic process of $Cs_3Bi_2I_9$/ZIF-8.

When $Cs_3Bi_2I_9$/ZIF-8 is exposed to visible light, a large number of electrons and holes are generated in $Cs_3Bi_2I_9$, and the electrons in the valence band (VB) are excited to the conduction band (CB) while the holes are left in the VB. As shown in Equation (2), ZIF-8 cannot be photoexcited here due to its large band gap. Due to the close contact at the heterojunction interface between ZIF-8 and $Cs_3Bi_2I_9$, electrons are spontaneously transferred from $Cs_3Bi_2I_9$ (E_{CBM} = −0.39 eV) to ZIF-8 (E_{CBM} = −0.35 eV). The value of −0.35 eV is lower than the potential of $O_2/\bullet O_2^-$ (−0.33 eV); therefore, the light-generated electrons can react with dissolved O_2 to form strongly oxidizing $\bullet O_2^-$ at the interface. The superoxide radical ($\bullet O_2^-$) preferentially oxidizes the thioether group (-S-) and amino group [-$N(CH_3)_2$] of MB, converting them into sulfoxide (-SO-) and sulfone (-SO_2^-) groups, thereby destroying the phenothiazine ring conjugation structure and generating open-ring intermediates. These open-ring products undergo hydroxylation and decarboxylation reactions to gradually release CO_2, forming small-molecule acids such as formic acid and oxalic acid, ultimately mineralizing into CO_2 and H_2O. Since the results show that in

our experiment only electrons and $\bullet O_2^-$ radicals play an important role [Figure 4f], the photodegradation process can be represented in Equations (3) and (4).

$$O_2 + e^- \rightarrow \bullet O_2^- \quad (3)$$

$$^*MB + \bullet O_2^- \rightarrow \text{mineralization products} \quad (4)$$

In addition to enhancing the electron transfer in $Cs_3Bi_2I_9$/ZIF-8, ZIF-8 can also provide abundant active sites and increase the contact surface area between the active sites and MB, thereby facilitating the photocatalytic reaction. The E_{VBM} of $Cs_3Bi_2I_9$ is 2.01 eV, which is higher than the potential of H_2O/h^+ (1.99 eV), and however, the results in Figure 4f show that holes and •OH radicals barely take part in the photocatalytic process. Maybe it is because MB photodegradation is more likely to occur on the ZIF-8 surface of $Cs_3Bi_2I_9$/ZIF-8.

3. Experimental Sections

3.1. Chemicals

Cesium acetate (CH_3COOCs, 99.9%), 1-octadecene (ODE, 90%), iodotrimethylsilane (TMS-I, 97%), silver nitrate ($AgNO_3$, 99.99%) and potassium iodide (KI, 98%) were purchased from Roan (Dundee, UK). Bismuth acetate [$Bi(CH_3COO)_3$, 99.99%] was purchased from Bidepharm (Shanghai, China). Oleic acid (OA, AR) was purchased from Aladdin (Tokyo, Japan). Oleylamine (OLA, 70%) and benzoquinone (BQ, 97%) were purchased from Macklin (Shanghai, China). Hexane (C_6H_{14}, 97%, AR), isopropyl alcohol (IPA, 99.7%, AR), sodium sulfate anhydrous (Na_2SO_4, 99%, AR), ethanol anhydrous (C_2H_5OH, 99%, GR), acetone (CH_3COCH_3, 99.5%, AR), and MB trihydrate were purchased from Xilong Scientific (Shantou, China). Zinc nitrate hexahydrate [$Zn(NO_3)_2{\cdot}6H_2O$] was purchased from Xilong Scientific. 2-methylimidazole (2-MIM, $C_4H_6N_2$) was purchased from Macklin. Nafion solution (5%) was purchased from Chengxin Science and Technology (Beijing, China). The purified water was sourced from Wahaha (Hangzhou, China). All reagents and solvents were used as received without any further purification.

3.2. Synthesis of ZIF-8, $Cs_3Bi_2I_9$ and $Cs_3Bi_2I_9$/ZIF-8

Synthesis of ZIF-8: First, 0.66 g (8.04 mmol) 2-MIM was added to 14.3 mL (0.353 mol) methanol. Then, 0.3 g (1.008 mmol) $Zn(NO_3)_2{\cdot}6H_2O$ was added to 14.3 mL (0.353 mol) methanol, and the solution of 2-MIM in methanol was poured into the methanol solution of $Zn(NO_3)_2{\cdot}6H_2O$. The final mixture was stirred at 1000 rpm for 1 h and then allowed to stand for 24 h. After standing, the solution was centrifuged at 8000 rpm for 3 min. Subsequently, the precipitate was washed twice with methanol, centrifuged, and dried to obtain ZIF-8.

Synthesis of $Cs_3Bi_2I_9$ and $Cs_3Bi_2I_9$/ZIF-8: A total of 0.14 mmol cesium acetate, 0.2 mmol bismuth acetate, 1.5 mL (4.75 mmol) OA, and 0.37 mL (1.125 mmol) OLA were dissolved in 6 mL (0.01875 mol) ODE. The mixture was heated to 120 °C under N_2 atmosphere. After maintaining the temperature for 30 min, the solution temperature was raised to 150 °C and 0.2 mL (1.7 mmol) TMS-I was rapidly injected to react for 1 min. After that, it was cooled in an ice water bath for 30 s. It was centrifuged at 8000 rpm for 15 min to obtain the precipitate. The precipitate was dispersed in hexane and centrifuged at 5000 rpm for another 15 min, and finally the precipitate was collected and dried in an oven at 60 °C for 24 h to obtain $Cs_3Bi_2I_9$ powder. The synthesis process of $Cs_3Bi_2I_9$/ZIF-8 is similar and shown in Figure 6, only differing in the fact that ZIF-8 was added into the cesium acetate/bismuth acetate solution when the temperature was heated to 120 °C. The obtained $Cs_3Bi_2I_9$/ZIF-8 samples by adding 10, 20, and 30 mg ZIF-8 are, respectively, named as CZ-1, CZ-2 and CZ-3. If not specially noticed, $Cs_3Bi_2I_9$/ZIF-8 below stands for CZ-2.

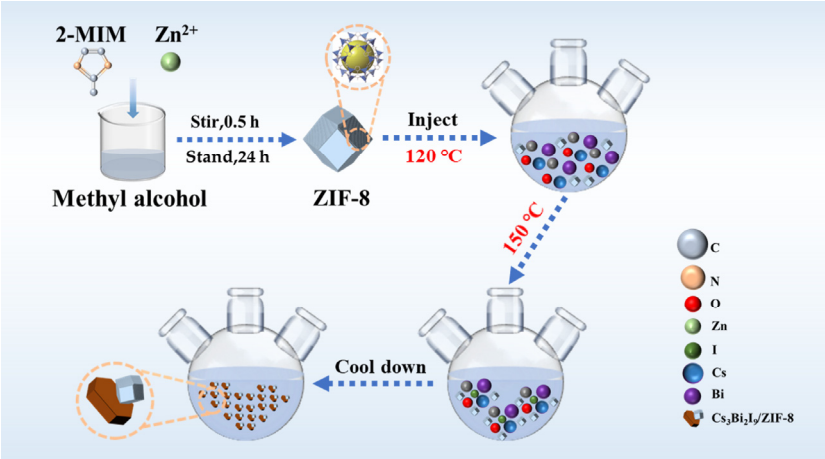

Figure 6. The synthesis process of $Cs_3Bi_2I_9$/ZIF-8.

3.3. Adsorption and Photocatalytic Test

The adsorption capacity of the sample was evaluated in the dark. First, add 20 mg sample (ZIF-8, $Cs_3Bi_2I_9$ or $Cs_3Bi_2I_9$/ZIF-8) to 50 mL MB solution (20 mg/L) and stir at a certain speed. At intervals of 1 h, 3 mL of the solution is withdrawn, and the concentration of MB was quantified using a UV-Vis spectrophotometer (Shimadzu UV-2700, Kyoto, Japan) by measuring its absorbance at 664 nm. The adsorption–desorption equilibrium of all the samples could be reached in 2 h. Visible-light photodegradation of MB (50 mL, 20 mg/L) was performed under xenon lamp (PLS-SXE 300, PerfectLight, Beijing, China, 300 W, $\lambda > 420$ nm). After the adsorption–desorption equilibrium was achieved, 3 mL of solution was withdrawn each time to measure the current concentration of MB at intervals of 10 min. The MB removal (including adsorption and photodegradation) efficiency was calculated with the formula [26]

$$\text{Removal efficiency } (\%) = \frac{C_0 - C}{C_0} \times 100\% = \frac{A_0 - A}{A_0} \times 100\%$$

where C_0 and C are the initial and real-time concentration of MB, respectively. A_0 and A represent the initial and real-time absorbance of MB at the wavelength of 664 nm, respectively. The recycling photodegradation tests were conducted by repeatedly collecting the photocatalysts through centrifugation at 8500 rpm and drying at 60 °C. Free radical capture experiments were conducted using IPA, $AgNO_3$, KI, and BQ as scavengers to determine the photocatalytic active species.

3.4. Electrochemical Tests

Transient photocurrents and electrochemical impedances were measured using a standard three-electrode electrochemical workstation (CHI 660E, Shanghai CH Instrument Company, Shanghai, China). The electrolyte was Na_2SO_4 solution (0.2 M), and the light source was a xenon lamp (PLS-SXE300, 300 W). Graphite electrode was used as the counter electrode, AgCl electrode as the reference electrode, and the sample as the working electrode. The photocatalyst was deposited onto the fluorine-doped tin oxide (FTO) electrode. A pristine FTO electrode was acquired through sequential soak and sonication in acetone, followed by deionized water washing and sonication in anhydrous ethanol. The mixture of 10 mg sample, 100 μL deionized water, 100 μL anhydrous ethanol and 30 μL nafion was sonicated for 20 min. Subsequently, the mixture was dropwise added using a pipette gun, consequently leading to the formation of an orange-red coating on the electrically charged side of the FTO electrode. After the resultant FTO electrode was dried in an oven, the sample-coating FTO electrode was then used for tests.

3.5. Characterization

The X-ray diffractometer (XRD, Miniflex 600, Rigaku, Tokyo, Japan) was used to study the crystal structure of $Cs_3Bi_2I_9$, ZIF-8 and the composite material $Cs_3Bi_2I_9$/ZIF-8. Its scanning angle ranged from 5 to 60°, with a scanning speed of 2°/min. The elemental compositions of ZIF-8, $Cs_3Bi_2I_9$ and $Cs_3Bi_2I_9$/ZIF-8 were characterized using an X-ray photoelectron spectrometer (XPS, Thermo Scientific K-Alpha, Waltham, MA, USA). The morphology of ZIF-8 was analyzed using scanning electron microscopy (SEM, TESCAN MIRA LMS, Brno, Czech Republic). The microstructures of $Cs_3Bi_2I_9$ and $Cs_3Bi_2I_9$/ZIF-8 were characterized and the lattice spacing was determined using high resolution transmission electron microscope (TEM, JEM-2100F, Hitachi, Tokyo, Japan). The valence electron structure of $Cs_3Bi_2I_9$ was measured using UV photoelectron spectroscopy (UPS, ESCALAB 250Xi, Thermo Scientific, Waltham, MA, USA). The UV-Vis absorption spectra of photocatalysts and organic pollutants were measured using a UV spectrophotometer (UV2700, Shimadzu, Kyoto, Japan), with the measurement wavelength range being 200~800 nm. The photoluminescence (PL) spectrum of the sample was measured using a fluorescence spectrometer (Edinburgh FL/FS900 Carry Eclipse, USA) from Agilent Technologies. An excitation wavelength of 380 nm is used, and the collected emission rage is 400–800 nm. The contact angle between $Cs_3Bi_2I_9$, $Cs_3Bi_2I_9$/ZIF-8 and water was measured by using SDC-200 angle measuring instrument of Dongwan Shengding Precision Instrument, Dongguan, China.

4. Conclusions

In summary, $Cs_3Bi_2I_9$/ZIF-8 photocatalysts with high catalytic activity were successfully prepared. The experimental results showed that the optimized $Cs_3Bi_2I_9$/ZIF-8 had a synergistic adsorption and photodegradation removal rate of MB up to 98.2%, which was better than most materials reported previously. The excellent photocatalytic performance is attributed to the efficient separation of photogenerated e-h pairs and electron transfer in $Cs_3Bi_2I_9$ by ZIF-8. In addition, it also advances in good water stability and reusability. The results also show that $\bullet O_2^-$ radicals are the main substances to oxidize MB in the photocatalytic degradation process. This work provides a promising strategy in the development of stable and cost-effective photocatalysts based on lead-free halide perovskites.

Author Contributions: T.T.; writing—review and editing, H.Z.; writing—original draft preparation, X.D. and H.Z.; data curation, H.W.; methodology and formal analysis, J.W.; investigation, L.J.; project administration, L.J.; funding acquisition. All authors have read and agreed to the published version of the manuscript.

Funding: This work was financially supported by the Natural Science Foundation of Guangxi Zhuang Autonomous Region (2025GXNSFAA069986), the Science and Technology Base and Talent Special Project of Guangxi Province (AD21220029), and the Research Foundation of Guilin University of Technology (GUTQDJJ2019011).

Institutional Review Board Statement: Not applicable.

Informed Consent Statement: Not applicable.

Data Availability Statement: The original contributions presented in this study are included in the article. Further inquiries can be directed to the corresponding author.

Conflicts of Interest: The authors declare no conflict of interest.

References

1. Saravanan, A.; Kumar, P.S.; Vo, D.-V.N.; Yaashikaa, P.R.; Karishma, S.; Jeevanantham, S.; Gayathri, B.; Bharathi, V.D. Photocatalysis for removal of environmental pollutants and fuel production: A review. *Environ. Chem. Lett.* **2020**, *19*, 441–463. [CrossRef]
2. Deng, F.; Shi, H.; Guo, Y.; Luo, X.; Zhou, J. Engineering paths of sustainable and green photocatalytic degradation technology for pharmaceuticals and organic contaminants of emerging concern. *Curr. Opin. Green Sustain. Chem.* **2021**, *29*, 100465.
3. Kumar, A.; Raizada, P.; Singh, P.; Saini, R.V.; Saini, A.K.; Hosseini-Bandegharaei, A. Perspective and status of polymeric graphitic carbon nitride based Z-scheme photocatalytic systems for sustainable photocatalytic water purification. *Chem. Eng. J.* **2020**, *391*, 123496.
4. Kumar, M.; Barbhai, M.D.; Puranik, S.; Radha; Natta, S.; Senapathy, M.; Dhumal, S.; Singh, S.; Kumar, S.; Deshmukh, V.P.; et al. Combination of green extraction techniques and smart solvents for bioactives recovery. *TrAC Trends Anal. Chem.* **2023**, *169*, 117286.
5. Yang, K.; Hao, L.; Hou, Y.; Zhang, J.; Yang, J.-H. Summary and application of Ni-based catalysts for electrocatalytic urea oxidation. *Int. J. Hydrogen Energy* **2024**, *51*, 966–981.
6. Yu, Y.; Lin, Z.; Liu, D.; Hou, Y. Exploring the spatially heterogeneous impacts of industrial agglomeration on regional sustainable development capability: Evidence from new energy industries. *Environ. Dev. Sustain.* **2023**, *26*, 16657–16682.
7. Rafiq, A.; Ikram, M.; Ali, S.; Niaz, F.; Khan, M.; Khan, Q.; Maqbool, M. Photocatalytic degradation of dyes using semiconductor photocatalysts to clean industrial water pollution. *J. Ind. Eng. Chem.* **2021**, *97*, 111–128.
8. Jia, P.; Tan, H.; Liu, K.; Gao, W. Adsorption behavior of methylene blue by bone char. *Int. J. Mod. Phys. B* **2017**, *31*, 1744099.
9. Theerthagiri, J.; Lee, S.J.; Karuppasamy, K.; Arulmani, S.; Veeralakshmi, S.; Ashokkumar, M.; Choi, M.Y. Application of advanced materials in sonophotocatalytic processes for the remediation of environmental pollutants. *J. Hazard. Mater.* **2021**, *412*, 125245.
10. Dai, H.; Yuan, X.; Jiang, L.; Wang, H.; Zhang, J.; Zhang, J.; Xiong, T. Recent advances on ZIF-8 composites for adsorption and photocatalytic wastewater pollutant removal: Fabrication, applications and perspective. *Coord. Chem. Rev.* **2021**, *441*, 213985.
11. Rojviroon, T.; Rojviroon, O.; Sirivithayapakorn, S. Photocatalytic decolourisation of dyes using TiO_2 thin film photocatalysts. *Surf. Eng.* **2016**, *32*, 562–569. [CrossRef]
12. Yildiz, S.; Canbaz, G.T.; Mihçiokur, H. Photocatalytic degradation of oxytetracycline using ZnO catalyst. *Environ. Prog. Sustain. Energy* **2024**, *43*, 14384. [CrossRef]
13. Sahu, K.; Satpati, B.; Mohapatra, S. Facile fabrication of CuO nanosheets for photocatalytic applications. *Appl. Phys. A* **2021**, *127*, 361. [CrossRef]
14. Uttam Pandit, V.R.; Parshuram Jadhav, G.K.; Sakharam Jawale, V.M.; Dubepatil, R.; Gurao, R.; Late, D.J. Synthesis and characterization of micro-/nano-α-Fe_2O_3 for photocatalytic dye degradation. *RSC Adv.* **2024**, *14*, 29099–29105. [CrossRef] [PubMed]
15. Maaß, M.C.; Tasch, A.; Jooss, C.; Waitz, T. Photocatalytic hydrogen evolution using ZnS particles and LEDs. *J. Chem. Educ.* **2022**, *99*, 2086–2092. [CrossRef]
16. Li, X.; Yu, J.; Wageh, S.; Al-Ghamdi, A.A.; Xie, J. Graphene in photocatalysis: A review. *Small* **2016**, *12*, 6640–6696. [CrossRef]
17. Donga, C.; Mishra, S.B.; Abd-El-Aziz, A.S.; Mishra, A.K. Advances in graphene-based magnetic and graphene-based/TiO_2 nanoparticles in the removal of heavy metals and organic pollutants from industrial wastewater. *J. Inorg. Organomet. Polym. Mater.* **2020**, *31*, 463–480. [CrossRef]
18. Fatima, R.; Warsi, M.F.; Zulfiqar, S.; Ragab, S.A.; Shakir, I.; Sarwar, M.I. Nanocrystalline transition metal oxides and their composites with reduced graphene oxide and carbon nanotubes for photocatalytic applications. *Ceram. Int.* **2020**, *46*, 16480–16492. [CrossRef]
19. Hong, X.; Wang, X.; Li, Y.; Fu, J.; Liang, B. Progress in graphene/metal oxide composite photocatalysts for degradation of organic pollutants. *Catalysts* **2020**, *10*, 921. [CrossRef]
20. Mehra, S.; Mamta; Tawale, J.; Gupta, G.; Singh, V.N.; Srivastava, A.K.; Sharma, S.N. Evaluating Pb-based and Pb-free halide perovskites for solar-cell applications: A simulation study. *Heliyon* **2024**, *10*, 33243. [CrossRef]
21. Thien, G.S.H.; Ab Rahman, M.; Yap, B.K.; Tan, N.M.L.; He, Z.; Low, P.L.; Devaraj, N.K.; Ahmad Osman, A.F.; Sin, Y.K.; Chan, K.Y. Recent advances in halide perovskite resistive switching memory devices: A transformation from lead-based to lead-free perovskites. *ACS Omega* **2022**, *7*, 39472–39481. [CrossRef]
22. Walker, B.; Kim, G.H.; Kim, J.Y. Pseudohalides in lead-based perovskite semiconductors. *Adv. Mater.* **2019**, *31*, 1807029.
23. Kwak, J.I.; Lee, T.-Y.; An, Y.-J. Assessing the potential toxicity of hazardous material released from Pb-based perovskite solar cells to crop plants. *J. Clean. Prod.* **2023**, *423*, 138856.
24. Zhu, Y.; Kang, Y.; Huang, H.; Zhuang, D.; Li, M.; Ling, Z.; Peng, K.; Zhai, L.; Zou, C. Systematic evaluation of the biotoxicity of Pb-based perovskite materials and perovskite solar cells. *J. Mater. Chem. A* **2024**, *12*, 2916–2923.
25. Guo, L.; Zhang, C.; Tan, T.; Li, L.; Qian, Q.; Mo, Y.; Lei, X.; Cai, W.; Wang, Z. Effect of band structure on the photocatalytic performance of $CsPbBr_3$/UiO-66 composites. *J. Solid State Chem.* **2024**, *339*, 124962.
26. Gu, Y.; Du, X.; Hua, F.; Wen, J.; Li, M.; Tang, T. Nitrogen-doped graphene quantum dot-passivated δ-phase $CsPbI_3$: A water-stable photocatalytic adjuvant to degrade rhodamine B. *Molecules* **2023**, *28*, 7310. [CrossRef]

27. Saparov, B.; Hong, F.; Sun, J.-P.; Duan, H.-S.; Meng, W.; Cameron, S.; Hill, I.G.; Yan, Y.; Mitzi, D.B. Thin-film preparation and characterization of $Cs_3Sb_2I_9$: A lead-free layered perovskite semiconductor. *Chem. Mater.* **2015**, *27*, 5622–5632.
28. Lee, L.C.; Huq, T.N.; MacManus-Driscoll, J.L.; Hoye, R.L.Z. Research update: Bismuth-based perovskite-inspired photovoltaic materials. *APL Mater.* **2018**, *6*, 084502.
29. Jain, S.M.; Edvinsson, T.; Durrant, J.R. Green fabrication of stable lead-free bismuth based perovskite solar cells using a non-toxic solvent. *Commun. Chem.* **2019**, *2*, 91.
30. Ghosh, B.; Wu, B.; Mulmudi, H.K.; Guet, C.; Weber, K.; Sum, T.C.; Mhaisalkar, S.; Mathews, N. Limitations of $Cs_3Bi_2I_9$ as lead-free photovoltaic absorber materials. *ACS Appl. Mater. Interfaces* **2018**, *10*, 35000–35007.
31. Liu, J.; Nie, W.; Yan, L.; Hu, H.; Zhang, G.; Lin, P.; Hu, H.; Xu, L.; Wang, P.; Cui, C. Anisotropic optoelectronic properties of lead-free $Cs_3Bi_2I_9$ single-crystal photodetectors. *J. Phys. D Appl. Phys.* **2024**, *57*, 335101. [CrossRef]
32. Zhang, R.; Chen, Z.; Ma, J.; Zhang, P.; Liu, M.; Li, X.; Zhao, R.; Tang, J.; Ren, Z.; Li, S. An all-solid-state photo-rechargeable battery based on $Cs_3Bi_2I_9$. *Chem. Commun.* **2023**, *59*, 2911–2914.
33. Lou, Y.; Fang, M.; Chen, J.; Zhao, Y. Formation of highly luminescent cesium bismuth halide perovskite quantum dots tuned by anion exchange. *Chem. Commun.* **2018**, *54*, 3779–3782.
34. Ji, J.W.; Zhang, L.J.; Yi, W.J.; Wang, Y.; Chen, J.H.; Yue, X.Z.; Yi, S.S. Re_3P_4@C/TiO_2 ohmic junction boosts charge carrier separation for photocatalytic hydrogen evolution. *Chem. Eng. J.* **2024**, *500*, 157277. [CrossRef]
35. Yali, Z.; Rong, W.; Aolin, L.; Jialei, H.; Zhilong, Z.; Shunhang, W. Constructing surface oxygen vacancy in the $[Bi_2O_2]^{2+}$ layer defects mediated Bi_2MoO_6 enhanced visible light responsive photocatalytic activity. *J. Chem. Phys.* **2024**, *161*, 184707.
36. Qiao, Y.N.; Zhang, Y.; Yuan, J.; Xue, H.M.; Jia, B. Construction of $NiCo_2S_4$/ZnCdS Schottky junction with unidirectional interfacial electron transfer for boosting photocatalytic hydrogen production. *ACS Appl. Energy Mater.* **2024**, *7*, 9921–9929. [CrossRef]
37. Tang, T.; Dou, X.; Zhang, H.; Wang, H.; Li, M.; Hu, G.; Wen, J.; Jiang, L. Enhancing the photocatalytic activity of lead-free halide perovskite $Cs_3Bi_2I_9$ by compositing with Ti_3C_2 MXene. *Molecules* **2024**, *29*, 5096. [CrossRef]
38. Chen, S.; Yin, H.; Liu, P.; Wang, Y.; Zhao, H. Stabilization and performance enhancement strategies for halide perovskite photocatalysts. *Adv. Mater.* **2022**, *35*, 2203836.
39. Fang, Z.; Yue, X.; Xiang, Q. Atomically contacted $Cs_3Bi_2Br_9$ QDs@UiO-66 composite for photocatalytic CO_2 reduction. *Small* **2024**, *20*, 2401914.
40. Zhang, Z.; Luo, X.; Wang, B.; Zhang, J. Electron transport improvement of perovskite solar cells via a ZIF-8-derived porous carbon skeleton. *ACS Appl. Energy Mater.* **2019**, *2*, 2760–2768.
41. Karim, M.R.; Choi, C.H.; Mohammad, A.; Yoon, T. Fabrication of high-performance supercapacitor of surface-engineered ZIF-8 for energy storage applications. *J. Energy Storage* **2024**, *93*, 112199.
42. Shi, Y.; Zhou, H.; Dai, L.; Liu, D.; Du, W. Preparation of ordered macroporous ZIF-8-derived magnetic carbon materials and its application for lipase immobilization. *Catalysts* **2024**, *14*, 55. [CrossRef]
43. Wang, Z.; Han, R.; Li, L.; Sun, J.; Yang, J.; Pan, M.; Wang, S. Electrochemical strategy based on the synergistic effect of ZIF-8 and MWCNTs for quantitation of tert-butylhydroquinone in oils and fried chips. *Microchem. J.* **2023**, *185*, 108268.
44. Ayyob, M.; Sun, Z.; Liu, Y.Y.; Wang, Y.; Wang, A. Performance of amine-modified CdS-D@ZIF-8 nanocomposites for enhanced photocatalytic H_2 evolution. *Int. J. Hydrogen Energy* **2023**, *48*, 25645–25659.
45. Karthieka, R.R.; Prakash, T. Dose-dependent X-ray sensing behaviour of $Cs_3Bi_2I_9$: PVDF-HFP nanocomposites. *Phys. E Low-Dimens. Syst. Nanostructures* **2021**, *133*, 114823.
46. Ta, D.N.; Nguyen, H.K.D.; Trinh, B.X.; Le, Q.T.N.; Ta, H.N.; Nguyen, H.T. Preparation of nano-ZIF-8 in methanol with high yield. *Can. J. Chem. Eng.* **2018**, *96*, 1518–1531.
47. Zheng, G.; Chen, Z.; Sentosun, K.; Pérez-Juste, I.; Bals, S.; Liz-Marzán, L.M.; Pastoriza-Santos, I.; Pérez-Juste, J.; Hong, M. Shape control in ZIF-8 nanocrystals and metal nanoparticles@ZIF-8 heterostructures. *Nanoscale* **2017**, *9*, 16645–16651.
48. Pramod, A.K.; Kushvaha, S.S.; Batabyal, S.K. Lead-free $Cs_3Bi_2I_9$ perovskite hexagonal microplates: A promising material solution-processed for ultraviolet self-powered photodetectors. *J. Alloys Compd.* **2024**, *1006*, 176320.
49. Pambudi, F.I. Electronic properties of heterometallic zeolitic imidazolate framework and its encapsulation with Ni, Pd and Pt. *Inorg. Chem. Commun.* **2022**, *143*, 109798.
50. Chen, X.; Chen, C.; Zang, J. Bi_2MoO_6 nanoflower-like microsphere photocatalyst modified by boron doped carbon quantum dots: Improving the photocatalytic degradation performance of BPA in all directions. *J. Alloys Compd.* **2023**, *962*, 171167.
51. Chen, X.; Chen, C.; Zang, J. Hybrid of carbon quantum dots modified g-C_3N_4 nanosheets and MoS_2 nanospheres: Indirectly promote hydroxyl group production for efficient degradation of methyl orange. *Diam. Relat. Mater.* **2023**, *139*, 110385.
52. Hong, Y.; Wang, B.; Hu, S.; Lu, S.; Wu, Q.; Fu, M.; Gu, C.; Wang, Y. Preparation and photocatalytic performance of Zn_2SnO_4/ZIF-8 nanocomposite. *Ceram. Int.* **2023**, *49*, 11027–11037.
53. Jing, H.P.; Wang, C.C.; Zhang, Y.W.; Wang, P.; Li, R. Photocatalytic degradation of methylene blue in ZIF-8. *RSC Adv.* **2014**, *4*, 54454–54462. [CrossRef]

54. Kitchamsetti, N.; Didwal, P.N.; Mulani, S.R.; Patil, M.S.; Devan, R.S. Photocatalytic activity of $MnTiO_3$ perovskite nanodiscs for the removal of organic pollutants. *Heliyon* **2021**, *7*, 07297.
55. Wang, Y.; Wang, L.; Liu, R.; Li, X. Casein templated synthesis of porous perovskite and its application in visible-light photocatalytic degradation of methylene blue. *Mater. Sci. Semicond. Process.* **2019**, *103*, 104597.
56. Bresolin, B.M.; Ben Hammouda, S.; Sillanpää, M. An emerging visible-light organic–inorganic hybrid perovskite for photocatalytic applications. *Nanomaterials* **2020**, *10*, 115. [CrossRef] [PubMed]
57. Kumar, M.; Vaish, R.; Elqahtani, Z.M.; Kebaili, I.; Al-Buriahi, M.S.; Sung, T.H.; Hwang, W.; Kumar, A. Piezo-photocatalytic activity of $Bi_2VO_{5.5}$ for methylene blue dye degradation. *J. Mater. Res. Technol.* **2022**, *21*, 1998–2012.
58. Tichapondwa, S.M.; Newman, J.P.; Kubheka, O. Effect of TiO_2 phase on the photocatalytic degradation of methylene blue dye. *Phys. Chem. Earth Parts A/B/C* **2020**, *118–119*, 102900.
59. Yao, M.; Yu, H.; Ding, K.; Du, Z.; Zhang, W.; Xia, Y.; Pan, X.; Wang, W.; Liu, X.; Li, S.; et al. Quantum dot/ZIF-67/ZIF-8 heterostructure for efficient photocatalytic hydrogen production. *ACS Appl. Nano Mater.* **2024**, *7*, 11445–11454.

Disclaimer/Publisher's Note: The statements, opinions and data contained in all publications are solely those of the individual author(s) and contributor(s) and not of MDPI and/or the editor(s). MDPI and/or the editor(s) disclaim responsibility for any injury to people or property resulting from any ideas, methods, instructions or products referred to in the content.